

SPECIAL ISSUE REVIEW ARTICLE

Diffusion MRI visualization

Thomas Schultz^{1,2}  | Anna Vilanova³ 

¹Bonn-Aachen International Center for Information Technology, Bonn, Germany

²Department of Computer Science, University of Bonn, Bonn, Germany

³Department of Electrical Engineering Mathematics and Computer Science (EEMCS), TU Delft, Delft, the Netherlands

Correspondence

A. Vilanova, Department of Electrical Engineering Mathematics and Computer Science (EEMCS), TU Delft, Delft, the Netherlands.

Email: a.vilanova@tudelft.nl

Modern diffusion magnetic resonance imaging (dMRI) acquires intricate volume datasets and biological meaning can only be found in the relationship between its different measurements. Suitable strategies for visualizing these complicated data have been key to interpretation by physicians and neuroscientists, for drawing conclusions on brain connectivity and for quality control. This article provides an overview of visualization solutions that have been proposed to date, ranging from basic grayscale and color encodings to glyph representations and renderings of fiber tractography. A particular focus is on ongoing and possible future developments in dMRI visualization, including comparative, uncertainty, interactive and dense visualizations.

KEYWORDS

diffusion MRI, diffusion tensor, tractography, visualization

1 | INTRODUCTION

Diffusion magnetic resonance imaging (dMRI) has provided unprecedented in vivo data on the structure of tissues such as brain white matter and muscle fibers. Visualization has become an essential tool for gaining insight into intricate dMRI data. At the same time, dMRI data have provided a challenging new application for scientific visualization research, which had previously focused on scalar volumetric data and vector fields. Diffusion tensor imaging (DTI) has been one of the driving applications for the visualization of tensor fields. Since then, imaging protocols and diffusion modeling have evolved and provide ever more complex information, such as distributions on the sphere or volumetric probability densities per voxel, which continues to pose challenges for visualization.

Several previous surveys have summarized the state of the art regarding dMRI visualization, focusing initially on DTI¹ and more recently on a wider range of dMRI models.² The overview in our article includes the most recent developments, puts a special focus on aspects that are complementary to previous surveys and reflects currently ongoing research, such as uncertainty or comparative visualization. An area of ongoing work that we decided to omit is the visualization of connectivity networks. These methods are less specific to diffusion MRI, since similar graph-based models are also used in other modalities, such as functional MRI, and a careful explanation of the underlying concepts would not be possible within the available space. We refer the interested reader to other recent surveys that include this topic.^{3,4}

The structure of our survey is as follows. In Section 2, we introduce visualization strategies that reduce the complicated dMRI data to a single grayscale or color. In Section 3, we focus on glyph visualizations, which allow for a more complete visualization of the available information. In Section 4, we discuss different visualization strategies for the results of tractography techniques. In Section 5, modifications of volume rendering and surface extraction techniques for dMRI data are reviewed. Finally, Section 6 presents the conclusions and an outlook on future research in dMRI visualization.

2 | GRAYSCALE AND COLOR ENCODINGS

Established visualization techniques are available for 3D grayscale or color images. Radiologists are trained to read series of 2D slice images. Volume rendering, isosurfaces or ridge surfaces are also used to show three-dimensional structures directly. An overview of these standard visualization techniques is given by Preim and Botha.⁴

Abbreviations used: dMRI, diffusion magnetic resonance imaging; DTI, diffusion tensor imaging; FA, fractional anisotropy; GPU, graphics processing unit; HiFIVE, Hilbert Space Embedding of Fiber Variability Estimates; HOME, higher-order maximum enhancing; LIC, line integral convolution; MD, mean diffusivity; ODF, orientation distribution function; ROI, region of interest; TDI, track-density imaging

Thomas Schultz and Anna Vilanova are in alphabetic order and both authors contributed equally.

It is not straightforward to apply such techniques to images from diffusion MRI, since diffusion is a three-dimensional process and is therefore modeled as a tensor, a distribution on the sphere or a 3D diffusion propagator, i.e. a 3D probability density function. At each point in space, dMRI acquires more information than can be encoded in a single grayscale or color value. Despite this, mapping at least some relevant aspects of the data to grayscale or color is a simple and widely used strategy for dMRI visualization.

1. Scalar invariants

Scalars for dMRI visualization are commonly defined to be invariant under rotations of the frame of reference, so that they capture intrinsic properties of anatomy rather than how subjects are positioned in the scanner. When the diffusion tensor model is used, invariance can be achieved by defining measures in terms of its eigenvalues, which are commonly sorted such that $\lambda_1 \geq \lambda_2 \geq \lambda_3$.

The most widely used measures in diffusion tensor imaging, shown in Figures 1(A) and (B), are fractional anisotropy (FA), which is normalized to $[0, 1]$ and quantifies the extent to which diffusion is isotropic (the same in all directions; FA=0) or directionally dependent (FA=1 when restricted to a single direction),⁵ and mean diffusivity (MD), which quantifies the overall amount of diffusion.

Other popular scalar measures include axial diffusivity $\lambda_{\parallel} = \lambda_1$ and radial diffusivity $\lambda_{\perp} = (\lambda_2 + \lambda_3)/2$, which assume a roughly axially symmetric tensor $\lambda_1 \gg \lambda_2 \approx \lambda_3$. An intuitive depiction of a diffusion tensor, shown in Figure 2(B) and discussed in more detail in Section 1, is an ellipsoid that shows the directional dependence of the diffusion. The ellipsoid is built by aligning the axes with the eigenvectors and scaling with the eigenvalues. Westin et al.⁶ propose to characterize these ellipsoids with three measures, c_l , c_p and c_s , reflecting the extent to which they are roughly linear, planar or spherical in shape. A barycentric space is spanned by these extremes and illustrated in Figure 3(A). Maps of these measures are shown in Figures 1(B)–(D). Linear shapes lead to high values of FA as well as c_l ; planar ellipsoids will cause low values of c_l , but can still correspond to values of FA up to $\sqrt{1/2}$ (see Figure 3A). Therefore, FA analysis is often complemented by a tensor mode,⁷ which reflects the continuum between linear (prolate; mode = 1) and planar (oblate; mode = -1) ellipsoids.

Many other scalar invariants have been derived based on more complex physical and microstructural models of diffusion MR data. Since it would exceed our scope to provide a complete list and a survey of microstructural models is given within this issue by Novikov et al.,⁸ we will only mention a few widely used measures that are based on the diffusion propagator.

The diffusion propagator is a three-dimensional probability density function that captures the local probability of certain molecular displacements during the diffusion time. From it, scalars such as the probability for zero displacement, i.e. the return to origin probability (RTOP, shown in Figure 1(C)), as well as the mean squared displacement,⁹ can be derived.

The diffusion tensor model corresponds to the assumption that the propagator can be expressed as a Gaussian distribution. Diffusional kurtosis can be used to quantify the extent to which the true propagator deviates from Gaussianity¹⁰ and introduces mean, axial and radial kurtosis as additional scalar invariants. Figures 1(G)–(I) map these based on the equations from Tabesh et al.¹¹; slightly different definitions exist in the literature.^{12,13} Similar to measures of diffusivity, measures of diffusional kurtosis are affected by both microstructural changes and fiber crossings.¹⁴

2. Color schemes for orientation

A widely used color scheme for estimated fiber directions maps the magnitude of the x , y and z components of the direction vector to the brightness of the red, green and blue color channels, respectively (XYZ-RGB).¹⁵ This makes it easy to recognize tracts that run left-to-right (red), front-to-back (green) or top-to-bottom (blue), but impossible to distinguish between many oblique directions, cf. Figure 2. Even though it is impossible to create a continuous color mapping that avoids such ambiguities fully, alternative schemes have reduced them to a minimum (in mathematical terms, to a set of measure zero¹⁶) or adapt the coloring to specific regions of interest¹⁷ to make more effective use of the available spectrum.

3 | GLYPHS

Glyphs, within the context of visualization, are iconographic or geometrical representations of the different variables from a data set.¹⁸ Glyphs show multi-dimensional information by encoding the different dimensions into properties such as shape or color. In contrast to the visualization techniques discussed in the previous section, glyphs allow us to visualize the full information available at a given point. The main limitation of glyph representations is that they put the focus on local information, which makes it more difficult to deduce global structures like fiber trajectories. It can be seen in Figure 4(A) that this is especially problematic when placing glyphs on regular grids. Creating an irregular packing via energy minimization, as in Figure 4(B), improves upon this by drawing more attention to continuous anatomical structures than to the discrete sampling pattern.¹⁹

1. DTI glyphs

Diffusion tensors can be represented as symmetric 3×3 matrices \mathbf{D} and thus have six degrees of freedom. Tensor glyphs allow us to visualize the full six-dimensional information. The most straightforward glyph representation of a diffusion tensor is an ellipsoid²⁰ that is defined as the set

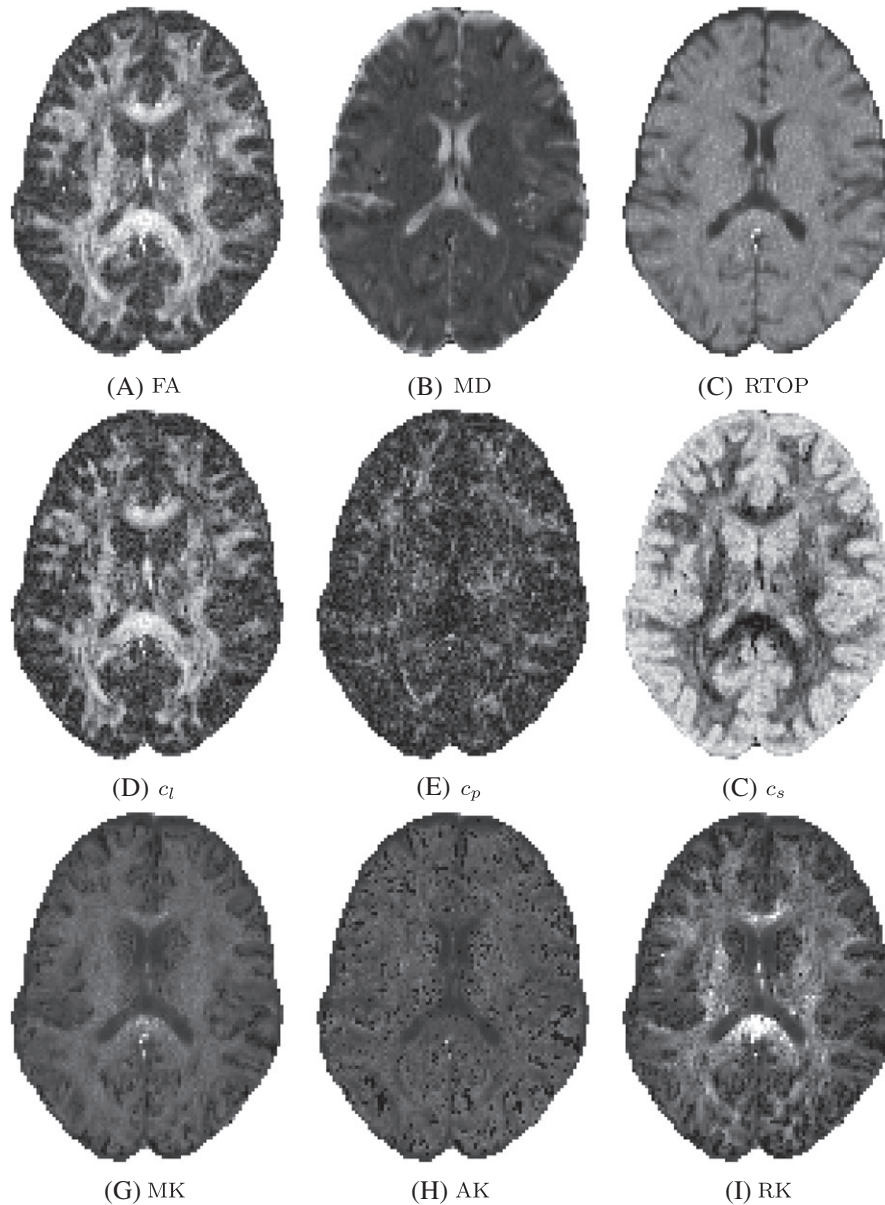


FIGURE 1 Scalar maps of diffusion MRI data can be created by modeling it with diffusion tensors (A, B, D, E, F), diffusional kurtosis (G, H, I) or diffusion propagators (C)

$\{x|x^T D^{-2} x = 1\}$; see Figures 2(B) and 4(A). The axes of these ellipsoids are aligned with the eigenvectors and scaled by the eigenvalues, which makes them easy to interpret.

It has been proposed that, compared with ellipsoids, boxes and cylinders make it easier to identify the main directions due to their sharper edges. Another alternative was proposed by Westin et al.⁶ and was formed by combining a stick scaled by c_l , a disk scaled by c_p and a sphere scaled by c_s .

It is important that the user obtains the necessary information from a visual encoding and is not misled by it. In tensor glyph design, properties that are relevant to fulfil this goal have been identified as symmetry, continuity and disambiguity.²¹ Symmetry relates to the fact that eigenvectors have no sign and that, if two eigenvalues are the same, the rotation of the glyph in the space spanned by their eigenvectors should not change the glyph. Boxes clearly violate this condition by showing arbitrary eigenvectors in the case of repeated eigenvalues. For continuity, slight changes in the tensor should be reflected as slight changes in the glyph. This is violated by cylinders, which require a sudden flip of the axis halfway between the linear and planar cases. Disambiguity means that different tensors should be easy to distinguish. This last property is not fulfilled by ellipsoids since, up to surface shading, quite different 3D ellipsoids can project to the same ellipse in the two-dimensional image.

Kindlmann²² proposed a superquadric glyph representation that meets these requirements by interpolating between spheres, cylinders and boxes, as shown in Figures 2(C) and 4(B). These glyphs fulfil all properties and are considered the state of the art for glyph-based tensor visualization. Fast generation of the glyphs is important for appropriate interaction. Pre-computed lookup tables of glyph shapes²¹ or ray casting²³ can be used for acceleration.

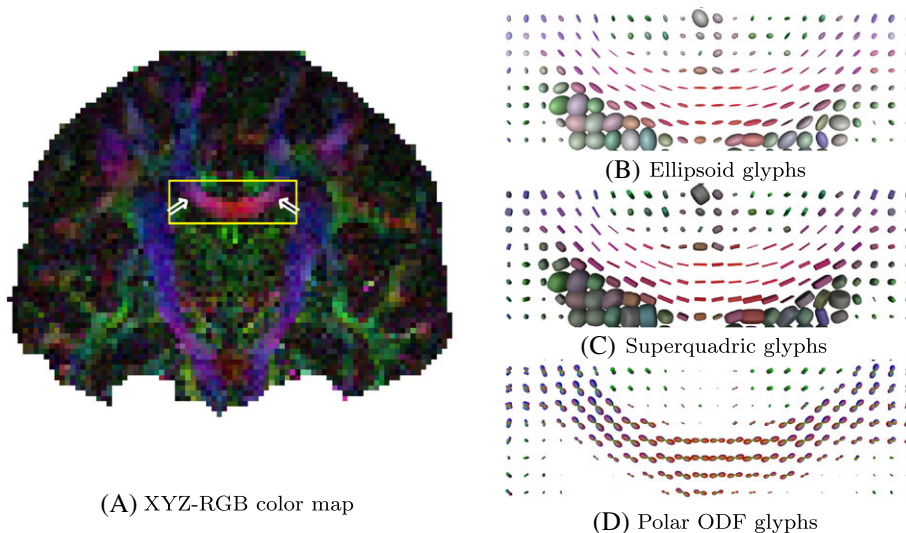


FIGURE 2 A. The XYZ-RGB color code provides a quick overview of main diffusion directions. B-D. As can be seen from the glyph visualizations, similar colors (arrows in A) are sometimes assigned to quite different orientations. The area for which glyphs are shown is indicated by the yellow box in A

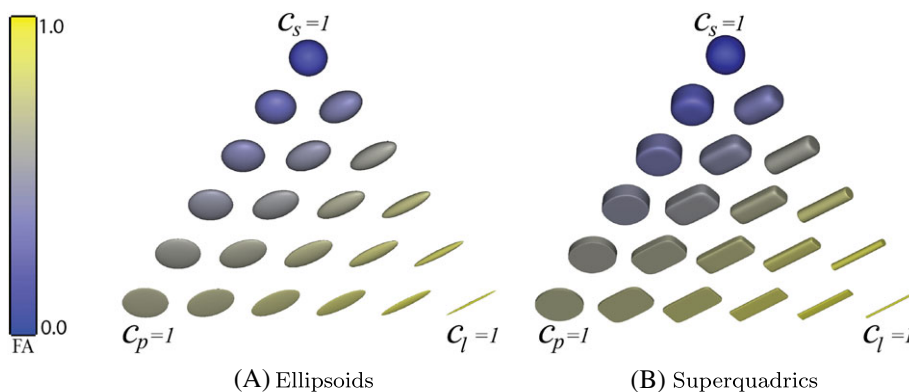


FIGURE 3 Westin's barycentric space of tensor shapes, color coded according to FA. A, Ellipsoids. B, Superquadric glyphs

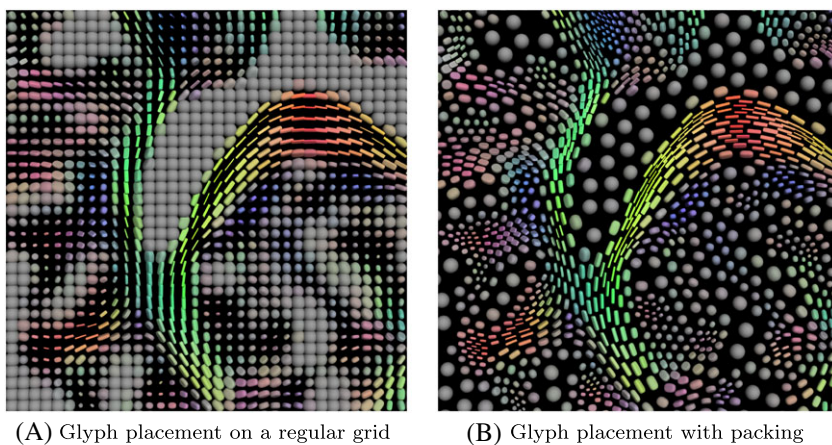


FIGURE 4 A, A regular placement. B, Compared with this, glyph packing emphasizes visually continuous anatomical structures more than the discrete sampling grid. Images kindly provided by Gordon Kindlmann (University of Chicago)

2. ODF glyphs

If multiple fiber populations are present within the same voxel, the diffusion tensor model cannot capture their individual orientations. Therefore, two families of orientation distribution functions (ODFs) have been introduced. Diffusion ODFs specify the overall amount of diffusion in a given direction, integrated over all displacement magnitudes.^{24,25} Fiber ODFs typically arise from deconvolution approaches and specify the fraction of fibers that run in a given direction.²⁶

In both cases, ODFs are density functions $\phi(\mathbf{u})$ on the sphere. The most widely used ODF glyph, shown in Figures 2(D) and 5(A), is constructed by scaling each point \mathbf{u} on the unit sphere according to the value $\phi(\mathbf{u})$. It generalizes the Reynolds glyph used in geomechanics²⁷ and is known under different names in the context of ODFs, including '(spherical) polar plot',^{24,25} 'parametrized surface'²⁸ or 'HARDI glyph'.²⁹ Even though ODFs generally exhibit antipodal symmetry $\phi(\mathbf{u}) = \phi(-\mathbf{u})$, this glyph can also be used for ODF-like objects with no such symmetry.^{30,31}

Peaks in the polar plot are often taken to indicate major fiber directions and the perception of their directions is often enhanced by color coding each surface point with the standard XYZ-RGB scheme.²⁴⁻²⁶ Optionally, the number and directions of ODF maxima can be emphasized by color coding each point according to its associated maximum rather than its own direction and the fact that broader peaks result in a greater directional uncertainty can be accounted for by modulating saturation according to the curvature.³² These two strategies are compared in Figures 5(A) and (B).

The angular contrast in some types of ODFs is subtle and it can make sense to enhance it visually by mapping the minimum and maximum radius to fixed values.²⁵ In other models, the absolute magnitude of ODF values carries relevant information and should thus be preserved in the visualization.³³

Generating polar plots is straightforward. However, displaying many of them at interactive frame rates requires specific techniques from computer graphics, such as Graphics Processing Unit (GPU)-based ray-casting^{29,34} or levels of detail and view frustum culling.³² An alternative way to enable interactive exploration, including remotely via network connections, is to pre-compute a large set of slice images.³⁵

Creating polar plots from diffusion tensors results in 'peanut-shaped' diffusivity profiles rather than the more widely used ellipsoids.²⁸ A direct generalization of tensor ellipsoids has been formulated based on a higher-order tensor representation of ODFs.³⁶ Since the resulting shapes exhibit sharper maxima than polar plots, they have been named higher-order maximum enhancing (HOME) glyphs.³² Figure 5 presents a direct comparison between polar plots (A,B) and HOME glyphs (C).

3. Glyphs for comparative visualization

The glyph visualizations presented until now provide the full information at a local position in one individual data set. However, there are many cases in which the interest is in identifying the differences between multiple data sets, rather than just visualizing a single one. Some such applications are understanding the relationship between acquisition protocols and diffusion models, the identification of differences in diffusion characteristics due to pathologies or the evaluation of registration or filtering algorithms.

Comparative visualization refers to the use of visual representations to understand the differences and similarities between two or multiple data sets. The main general strategies³⁷ are juxtaposition, superposition and explicit encoding. Juxtaposition is setting two images side by side and is used most commonly. It is straightforward to implement, but relies on the viewer's memory, which makes it challenging to notice all differences. For instance, Hotz et al.³⁸ used juxtaposition to compare interpolation schemes and Schultz et al.³⁹ juxtaposed to compare the uncertainty variation between two acquisition schemes with different echo times.

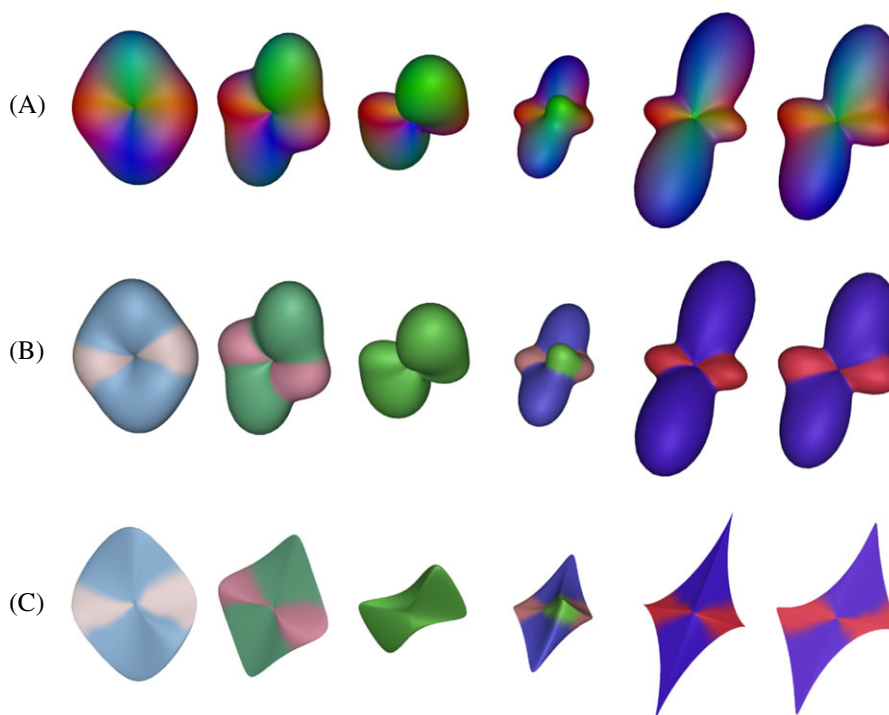


FIGURE 5 A. ODFs are most frequently rendered as polar plots. B. Points are colored according to the associated maximum to emphasize number and directions of peaks visually; saturation is reduced for broader peaks. C. Higher-order maximum enhancing glyphs generalize diffusion tensor ellipsoids and indicate the directions of peaks more precisely through their sharper shape

Superposition puts objects in the same frame of reference. It provides direct comparison but suffers from occlusion and visual clutter; see Figure 6(A). As discussed by Zhang et al.,⁴⁰ transparency can alleviate occlusion; however, interpretation remains challenging. Examples of the superposition strategy can be seen in Jones et al.⁴¹ based on the ellipsoid glyph. Recently, Abbasloo et al.⁴² presented a strategy in which glyphs are rendered in complementary colors and composed in image space to improve the perception of differences.

Explicit encoding involves computing and visually encoding the differences directly. Zhang et al.⁴⁰ designed the Tender ('tensor difference') glyph to analyze the differences between two second-order tensors, identifying the separate factors that contribute to the differences. A symmetric second-order tensor can be decomposed into three components: tensor scale, shape and orientation, which are easy to interpret.⁷ Tender glyphs use a coherent way to calculate the distance explicitly for each of these factors. The visual encoding is based on a checkerboard pattern for the shape, color for the scale and an angle glyph for the orientation, as shown in Figure 6(C).

4. Glyph encodings of uncertainty

Noise in diffusion MR measurements propagates through the modeling pipeline and results in uncertainty in derived quantities, including fiber directions, diffusion tensors and orientation distribution functions. This uncertainty can be estimated from repeated acquisitions or with model-based bootstrapping.⁴³ Visualizing the uncertainty can help assess measurement precision, which often varies throughout the brain, and guide selection of acquisition schemes and models.

Fiber directions are among the main parameters of interest that are derived from diffusion MRI. Visualizing uncertainty in those directions is similar to visualizing uncertain vector fields, for which a range of glyph-based techniques exist.⁴⁴ In diffusion MRI, cones of uncertainty are a popular depiction, indicating the main direction and a confidence interval around it.⁴⁵

Figure 7 compares such cones of uncertainty with the HiFiVE glyph, which instead indicates a main direction (as colored double cones) and a density estimate of the uncertainty around it (as a gray surface). This reveals asymmetries in uncertainty that remain hidden when using cones. The name HiFiVE stems from the mathematical derivation, from a Hilbert Space Embedding of Fiber Variability Estimates.³⁹ When multiple fiber compartments are modeled within the same voxel, the Expectation Maximization algorithm can be used to ensure that this does not inflate estimates of uncertainty in their individual directions.⁴⁶

Depicting the full uncertainty in the diffusion tensor is a far more complex task, since it affects not only eigenvectors but also properties such as mean diffusivity and anisotropy. Moreover, variations in different properties might be correlated with each other. Bassler et al.⁴⁷ propose to model this with a tensor normal distribution and they derive a glyph representation of the overall variance in each direction, as well as a composite glyph that depicts the eigentensors of the fourth-order covariance. Abbasloo et al.⁴² argue that it is more intuitive to display how the principal modes of variation affect a specific diffusion tensor. Therefore, they add ± 3 standard deviations along each mode to the mean tensor and overlay the resulting glyphs.

Since orientation distribution functions have even more degrees of freedom than diffusion tensors, it becomes increasingly difficult to estimate their complete variance and covariance reliably and to visualize it in an interpretable manner. Jiao et al.⁴⁸ present an initial approach to this problem, which estimates and volume-renders the probability of each point being on the inside of a polar ODF glyph.

4 | FIBER TRACKING

Fiber tracking or tractography reconstructs the trajectories of major white matter tracts. A variety of algorithms for fiber tracking have been proposed and are surveyed by Jeurissen et al.⁴⁹ within this issue. In the following, we will focus on how to visualize the results of tractography, starting with the most widely used streamline-based and dense representations, then moving on to streamsurfaces, visual encodings of uncertainty and techniques that visualize fiber bundles as a whole.

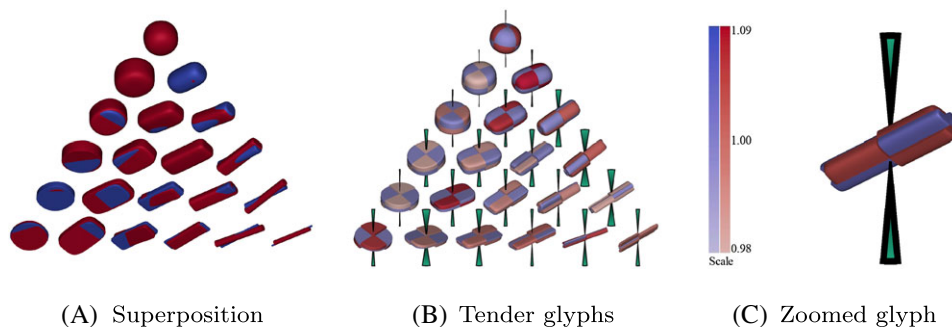


FIGURE 6 Example of comparative visualization techniques for two synthetic data sets identified in red and blue, one of which is shown in Figure 3. A. Superposition of two data sets. B. Tender glyphs in the barycentric space. C. Detail view of an individual tender glyph. Differences in shape are visible in the checkerboard pattern, luminance encodes scale and an angle glyph explicitly encodes the difference in orientation

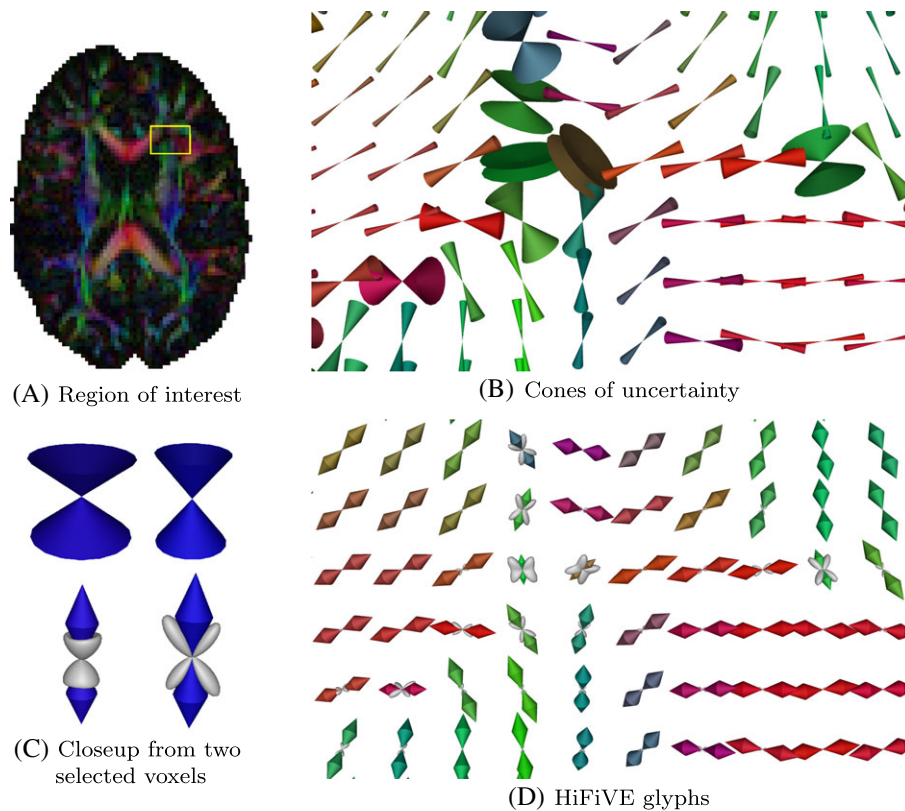


FIGURE 7 A. Region of interest. B. Cones of uncertainty show a 95% confidence angle around the mean fiber direction. C. A closeup illustrates that cones (top) always suggest cylindrical symmetry, while the gray surfaces from the HiFiVE glyphs (bottom) distinguish between symmetric (left) and unsymmetric cases (right), where uncertainty is highest within some plane. D. HiFiVE glyphs visualize possible alternative directions as a density estimate around the main direction

1. Streamline rendering

Fiber tracking results in curves that are most commonly rendered as thin lines,⁵⁰ illuminated streamlines⁵¹ or cylindrical tubes,⁵² the shading of which helps to convey their three-dimensional trajectories (see Figure 8).

When using the diffusion tensor model, streamtubes have been used to encode information about the second and third eigenvector fields in cross-sectional shapes such as cross shapes, ellipses⁵⁴ (see Figure 8E) and superquadrics.⁴⁶ They had previously been proposed for the visualization of tensor fields in solid mechanics and fluid dynamics, where they were called hyperstreamlines.⁵⁵ Color⁵⁴ and texture^{56,57} have been used as additional visual channels.

Models for multi-fiber tractography contain even richer information at each point in space. It has been visualized by placing ODF glyphs along the curve⁵⁸ or by creating hyperstreamlines with cross-sections indicating secondary fiber directions.⁵⁹

In streamline visualizations, the number and placement of curves are important factors, since using too many leads to visual clutter, while relevant structures might be missed when using too few or placing them inadequately.⁶⁰ Strategies that have addressed this within the context of diffusion imaging include a dense initial sampling, based on which a smaller set of long and representative streamlines is selected,⁵⁴ and a greedy strategy that seeds new streamlines incrementally sufficiently far away from all existing ones and terminates them if they come too close to an existing one.⁶¹

To achieve interactive frame rates when rendering results from whole-brain tractography, the programmable shader units on modern graphics hardware can be used to achieve the visual impression of cylindrical tubes despite the use of greatly simplified planar geometry.⁵⁶ This has been done using iterative ray casting⁶² or textures that emulate exact shading⁶³ or by mixing techniques depending on the level of detail.⁵⁷

Even though local surface shading conveys surface orientation, the visual complexity of tractography images can make it difficult to recognize exact three-dimensional structures and the spatial relationship of different fibers to each other. Therefore, cues from global illumination, such as physically realistic⁶⁴ or real-time approximative shadows,⁶⁵ have been added (see Figure 11A). Alternatively, illustrative techniques, such as rendering curves completely in black and using haloes to convey their depth ordering,⁶⁵ have drawn their inspiration from traditional medical illustration.⁶⁷

Initial attempts have been made to use immersive virtual environments⁶⁸ or large and stereoscopic screens to improve tractography visualization, but it has so far proven difficult to demonstrate a clear benefit in terms of task accuracy or completion time.⁶⁹

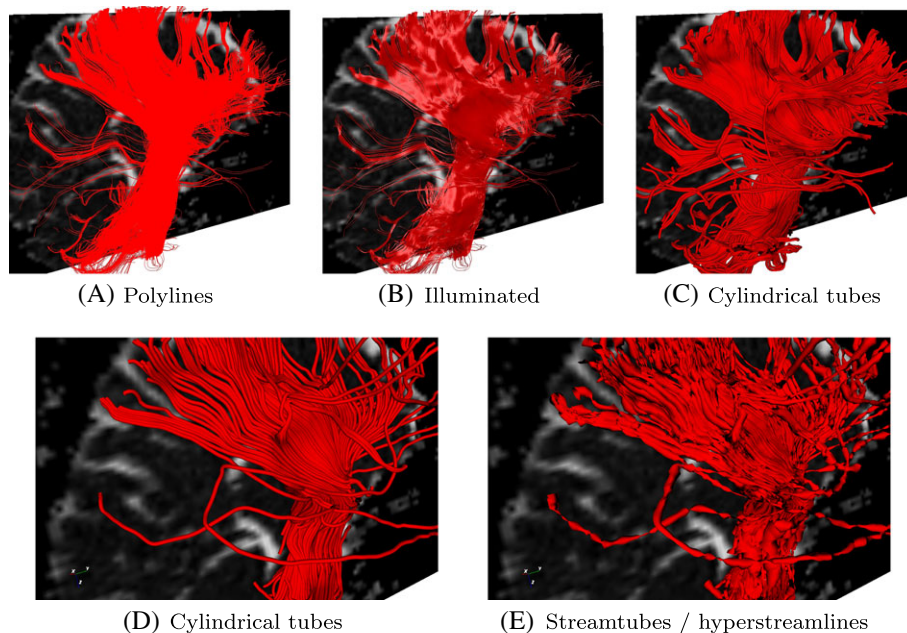


FIGURE 8 Illustration of different visualization alternatives for tractography results. Images generated using vIST/e⁵³

2. Dense visualization

Streamline tractography results are highly dependent on seeding strategies. In contrast, dense visualizations display information everywhere, without dependence on seeding. In this section, we will present dense visualizations derived from fiber tractography, in analogy to methods from flow visualization that are called dense or texture-based.⁷⁰

Spot noise⁷¹ and line integral convolution (LIC)⁷² are the first published techniques on dense flow visualization. LIC is the most popular and is based on synthetically generated noise images that are convolved along characteristic curves of the vector field; see Figure 9(A). A multitude of extensions of these approaches exist, such as computational optimizations^{73,74} and extensions to tensor fields.^{75,76} Even though generalization to 3D exists,^{77,78} dense visualization techniques are most effective for 2D, since for 3D occlusion becomes a severe problem.

LIC has been applied in cardiac DTI along the two principal eigenvector directions to visualize the sheet structure of the myocardium⁷⁹ and in brain DTI either along the major eigenvector field⁸⁰ or, in a multi-pass fashion, along all eigenvector fields.⁷⁵ More recently, it has also been used to texture surfaces⁸¹ and been extended to multiple fiber directions.⁸²

Track-density imaging (TDI)^{83,84} is based on tracing a huge number of fiber tracts (e.g. 2.5 million) by seeding randomly throughout the whole brain and using probabilistic tractography. Then, a high-resolution grid is generated on top of the fibers and voxel intensities reflect the number of fiber tracks that go through each voxel. The idea of TDI is that global information from tractography allows for an increased resolution (i.e. super resolution). The resulting images are similar to histopathology results, which provide a good anatomical contrast,⁸⁴ shown in Figures 9(B) and (C). There is a strong similarity between TDI and LIC, if we consider the random seed locations in TDI as a sparse noise texture for LIC and assume a long and uniform convolution kernel.

3. Streamsurfaces

When using the diffusion tensor model, fiber tracking traces curves along the major eigenvector field and is limited to regions of linear tensor shapes ($\lambda_1 \gg \lambda_2 = \lambda_3$).

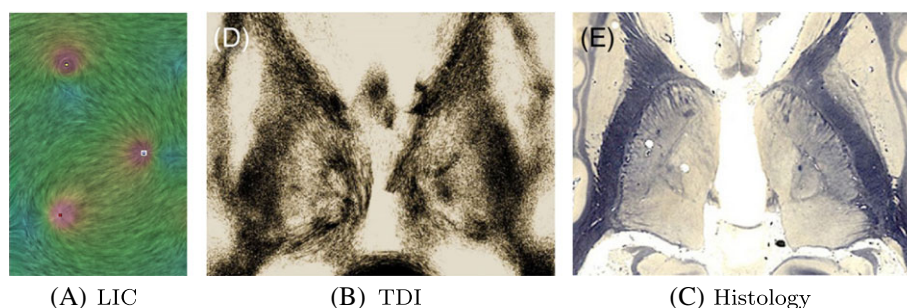


FIGURE 9 A. Example of LIC visualizations of a 2D flow field generated using IBFV⁷¹ B. TDI results at the level of the thalamus. C. The corresponding histological sections from a different subject in a similar area. Image obtained from Calamante et al.⁷²

As a seemingly natural extension, visualization of regions of planarity (i.e. $\lambda_1 \approx \lambda_2 \gg \lambda_3$) has been proposed by integrating surfaces that are everywhere tangential to the major and medium eigenvector fields. In analogy to streamlines, these surfaces have been named streamsurfaces⁵⁴ and have been combined with streamlines in a system for diffusion tensor tractography.⁶¹

It is worth noting that, in contrast to streamlines, streamsurfaces are only well-defined mathematically if the vector fields from which they are derived satisfy an integrability condition in terms of their Lie bracket.⁵⁴ Results in Schultz et al.⁸⁵ suggest that this condition is not met in all planar regions. As an alternative surface-based visualization of planar regions that does not depend on eigenvector integrability, ridge surfaces of Westin's c_p (cf. Section 1) can be shown.⁸⁵

Interestingly, it has been proposed recently that fiber pathways in humans and four nonhuman primates indeed form sheet structures.⁸⁶ Formally checking integrability is a topic of ongoing investigation.⁸⁷⁻⁸⁹

4. Visualizing uncertainty in tractography

The uncertainty in estimated fiber directions, which we discussed in Section 4, propagates into the results of fiber tractography. Measures of local uncertainty have been visualized by mapping them onto the cross-sections of streamtubes.^{46,90} Probabilistic tractography goes beyond such local models by capturing how uncertainty accumulates during tracking.⁹¹ For each seed point, it traces a large number of curves, for which visualization is challenging.⁹²

Superimposing all streamlines produced by a probabilistic technique does not convey a clear impression of which regions contain the most likely connections.^{93,94} Color-coding the probability with which streamlines from a specific seed region traverse a given voxel is another simple and widely used visualization,^{91,93-95} but one limited in its ability to convey three-dimensional shape.

Confidence intervals of three-dimensional bundle geometry have been recovered from sets of streamlines by constructing geometric hulls that wrap a varying fraction of streamlines,⁹⁶ based on topological analysis⁹⁷ and the assumption that the possible connections between two given endpoints are Gaussian-distributed.^{98,99} To reduce visual complexity, confidence intervals have also been rendered using illustrative techniques,¹⁰⁰ as shown in Figure 10(A).

Since there is no fully objective way of setting the stopping criteria that are part of most tractography methods, their choice constitutes another source of uncertainty. Brecheisen et al.¹⁰¹ present a system that can be used to explore their effect systematically and to identify regions in parameter space in which results are stable (see Figure 10B). A related work by Jiao et al.¹⁰² additionally accounts for parameters such as integration step size or the choice of tractography algorithm.

5. Interaction and bundle visualization

Despite the use of advanced rendering techniques,^{65,66} interpreting renderings of whole brain tractography as in Figure 11(A) remains challenging. The overwhelming amount of data being visualized makes it difficult to perceive shapes clearly and to interact with the large number of fibers.

To deal with clutter and occlusion, visualization systems often follow the strategy 'overview first, zoom and filter, then details on demand'.¹⁰³ It emphasizes the role of interaction to leverage the knowledge of the user, who is put in a position to identify, select and summarize information. In dMRI visualization, tracts are often seeded or filtered manually, e.g. by delineating regions of interest (ROIs) on 2D slices which show a color mapping (cf. Section 2). Fiber tracts can be included or excluded, depending on whether they pass through one or several ROIs.¹⁰⁴

In exploration systems, real-time interaction is of major importance. Blaas et al.¹⁰⁵ use acceleration techniques to allow for interactive selection of pre-computed fiber tracts through 3D widgets such as cubes. Techniques for real-time generation of tractography have also been proposed.^{106,107} Streamline selection beyond the use of ROIs has been explored for general flow visualization,¹⁰⁸ as well as for tractography. Tax et al.¹⁰⁹ presented a technique where visibility is determined by the orientation of fiber tracts in relation to the viewer. Sherbondy et al.¹¹⁰

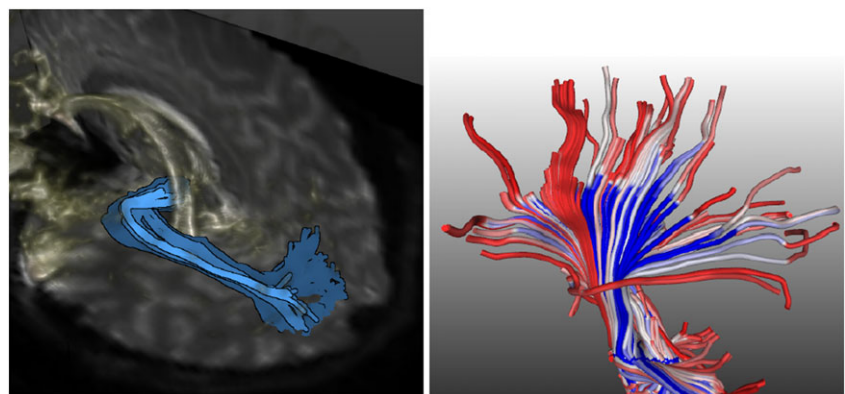


FIGURE 10 A. This illustrative rendering shows three different confidence intervals of the optic radiation, with a volume rendering for context.¹⁰⁰ B. Visualization of sensitivity to stopping criteria threshold for corona radiata streamlines. High variability in color indicates sensitivity to threshold.¹⁰¹ Images generated with vIST/e⁵³

developed a query language that allows selections based on characteristics beyond the fiber geometry, including additional information such as from functional MRI.

Since selecting fiber bundles in 3D views is challenging, Chen et al.¹¹¹ and Jianu et al.¹¹² use a 2D embedding in which fibers are represented by points, which are close to each other if the corresponding 3D streamlines are similar. In their system, selections are made in several linked 2D views, including the 2D embedding and dendrograms, and are reflected in a 3D view. Jianu et al.¹¹³ also developed a more intuitive representation of the 2D embedding.

A grouping of streamlines that has been achieved manually or using automated techniques^{114,115} is often conveyed by assigning one color per bundle, as in Figure 11(B). Alternatively, surfaces have been wrapped around the clustered fibers,^{96,116} which is challenging when bundles have complex geometries. Van Otten et al.¹¹⁷ propose a focus and context method where abstract illustrative techniques are used for the context bundles (see Figure 11C), while more detailed representations are used for the focus. Interaction with exploded views is presented to reduce the occlusion while preserving the context.

5 | VOLUME RENDERING

From 2D slice views, as shown in Section 2, the user has to reconstruct three-dimensional structures mentally, which is a tedious task even for trained users. Therefore, techniques that render the three-dimensional volume into a single image have been extended for diffusion MRI. Such volume-rendering methods are commonly divided into two categories: indirect volume rendering is based on first extracting geometric representations, while direct volume rendering produces images without such an intermediate representation.⁴

1. Indirect volume visualization

Indirect volume visualization is based on geometric representations, such as curves or surfaces. Since curves and surfaces from fiber tracking were already discussed in Section 4, we will now deal with complementary techniques, which are based on the scalar invariants from Section 2. A classical example is isosurfaces, i.e. sets of points at which a scalar field equals some constant isovalue. When applied to anisotropy measures, isosurfaces provide an outline of core white matter structures.¹¹⁸

Another example is ridges, which are located where a scalar field is locally maximal. Since FA tends to be largest at the center of fiber bundles, ridges in FA have been used to visualize what has been referred to as a white matter skeleton.¹¹⁹ Ridge curves and surfaces have been extracted based on Eberly's formalization.¹²⁰ Ridge surfaces as in Figures 12(C,E) capture sheet-like tracts, while ridge curves are more suitable for tubular tracts such as the cingulum bundle.¹²¹ Valley surfaces are located at local minima of FA and capture interfaces between adjacent, but differently oriented, bundles,¹¹⁹ as shown in Figures 12(B,D,F). To localize ridges reliably, one must account for differences in their spatial scale, which are caused by variations in the thickness of fiber bundles. Scale-space analysis can be used to extract ridges at the scale at which they are most salient.^{122,123}

FA ridges are closely related to the FA skeleton that is used for statistical analysis in tract-based spatial statistics.¹²⁴ In the latter case, skeletons are extracted in group-averaged FA maps using non-maximum suppression and are represented as sets of voxels rather than polygonal curves or triangle meshes.

2. Direct volume rendering

Direct volume rendering is based on defining a transfer function, which maps the data at each point to color and opacity. According to these values, the emission and absorption of light at each point is simulated and an image is captured with a virtual camera.¹²⁵ Transfer functions for data from diffusion tensor imaging have been defined based on Westin's measures,⁶ diffusion-tensor orientation or reaction-diffusion textures that can be generated from the diffusion tensors. Lighting computations that account for tensor anisotropy and orientation have also been used.¹²⁶

Direct volume rendering of diffusional kurtosis has been performed by multiplying the directionally dependent values of kurtosis with a local distribution of incoming light and integrating the result over the sphere to obtain color and opacity. When the incoming light depends on the eigenvectors of the diffusion tensor, this makes it possible to achieve an effect similar to visualizing axial or radial kurtosis.¹²⁷

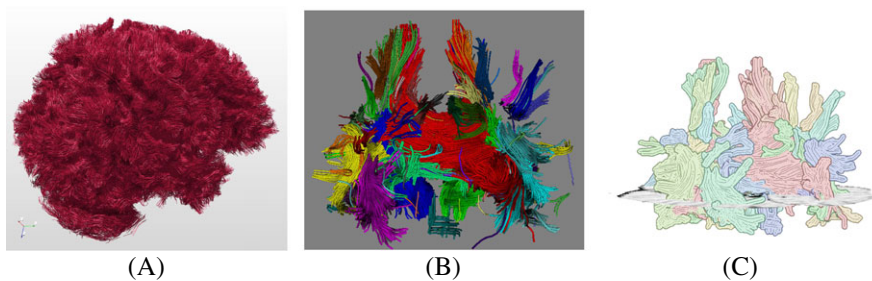


FIGURE 11 A. Full brain tractography rendering using illuminated streamlines and shadows. B. Traditional bundle visualization. C. Illustrative based bundle rendering from Otten et al.¹¹⁷ Images generated using vIST/e⁵³

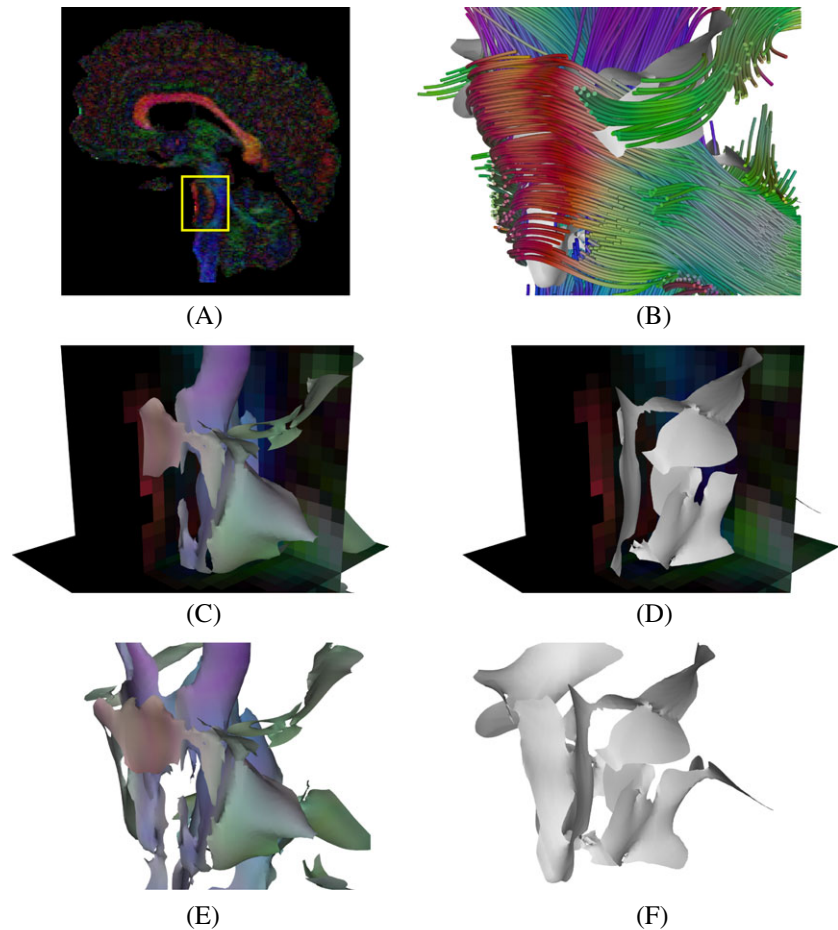


FIGURE 12 FA ridge and valley surfaces in the brainstem region, highlighted in A. FA ridges are surfaces of locally maximal FA and capture the cores of sheet-like tracts. They are illustrated (C) with and (E) without context from slice images. D, F. FA valleys are surfaces of locally minimal FA and separate nearby, but differently oriented fiber bundles. B. Illustration of this, in the context of tractography. Brain dataset courtesy of Gordon Kindlmann (University of Chicago) and Andrew Alexander (W. M. Keck Laboratory for Functional Brain Imaging and Behavior, University of Wisconsin-Madison)

6 | CONCLUSIONS AND OUTLOOK

Diffusion MRI provides intricate data that pose complex visualization challenges. Since information density is too high to encode the available data fully into a single image, we have discussed a set of complementary visualization techniques, each representing a different type of visual abstraction. Their combined interactive use is key to obtaining comprehensive insights.

The ongoing technical progress in dMRI continues to increase the complexity of the resulting data and pose new challenges for visualization.¹²⁸ Combined visualization of dMRI with other information such as from functional Magnetic Resonance Imaging (fMRI) will be relevant to gaining scientific insight, as well as for personalized treatment, e.g. in neurosurgery. Effective visualizations will be based on a careful analysis of these complex tasks. Facilitating access to the resulting visualization tools, e.g. through web-based solutions,^{35,129} is another important aspect.

Visualizing the uncertainty that arises from measurement noise or choice of models is important to avoid false conclusions. For scientific studies, it is important to connect visual and statistical tools for analyzing dMRI data, e.g. to compare healthy or patient populations and to identify biomarkers. Even though we summarized the work that has been done on uncertainty and group visualization so far, this line of research is still in its infancy.

Finally, structural connectivity networks can be derived from dMRI. Even though we had to exclude this topic from our survey, we expect to see more and important work on this in the future.

In summary, even though dMRI visualization has evolved considerably in the last two decades, facilitating better insight into dMRI data and creating images with aesthetic appeal to a wide audience,¹³⁰ we believe that important work is still ahead of us, both in terms of addressing the visualization challenges of new dMRI variants and models and in terms of techniques for statistical and comparative visualization, as well as for brain connectivity.

ORCID

Thomas Schultz  <http://orcid.org/0000-0002-1200-7248>

Anna Vilanova  <http://orcid.org/0000-0002-1034-737X>

REFERENCES

1. Vilanova A, Zhang S, Kindlmann G, Laidlaw D. An introduction to visualization of diffusion tensor imaging and its applications. In: *Visualization and Processing of Tensor Fields*. Berlin Heidelberg: Springer; 2006:121-153.

2. Leemans A. Visualization of diffusion MRI data. In: Jones D, ed. *Diffusion MRI*. Oxford: Oxford University Press; 2010:354-379.
3. Margulies DS, Böttger J, Watanabe A, Gorgolewski KJ. Visualizing the human connectome. *Neuroimage*. 2013;80:445-461.
4. Preim B, Botha C. *Visual Computing for Medicine: Theory, Algorithms, and Applications*. Amsterdam: Morgan Kaufmann; 2013.
5. Basser PJ, Pierpaoli C. Microstructural and physiological features of tissues elucidated by quantitative-diffusion-tensor MRI. *J Magn Reson, Ser B*. 1996;111:209-219.
6. Westin CF, Maier S, Khidhir B, Everett P, Jolesz F, Kikinis R. Image processing for diffusion tensor magnetic resonance imaging. In: *Proc. Medical Image Computing and Computer-Assisted Intervention (MICCAI); 1679 of LNCS*. Berlin Heidelberg: Springer; 1999:441-452.
7. Ennis DB, Kindlmann G. Orthogonal tensor invariants and the analysis of diffusion tensor magnetic resonance images. *Magn Reson Med*. 2006;55:136-146.
8. Novikov D, Jespersen S, Kiselev V, Fieremans E. Quantifying brain microstructure with diffusion MRI: Theory and parameter estimation. *NMR Biomed*. In this issue
9. Assaf Y, Mayk A, Cohen Y. Displacement imaging of spinal cord using q-space diffusion-weighted MRI. *Magn Reson Med*. 2000;44:713-722.
10. Lu H, Jensen JH, Ramani A, Helpert JA. Three-dimensional characterization of non-Gaussian water diffusion in humans using diffusion kurtosis imaging. *NMR Biomed*. 2006;19:236-247.
11. Tabesh A, Jensen JH, Ardekani BA, Helpert JA. Estimation of tensors and tensor-derived measures in diffusional kurtosis imaging. *Magn Reson Med*. 2011;65:823-836.
12. Hui ES, Cheung MM, Qi L, Wu EX. Towards better MR characterization of neural tissues using directional diffusion kurtosis analysis. *Neuroimage*. 2008;42:122-134.
13. Poot DHJ, Dekker AJ, Achten E, Verhoye M, Sijbers J. Optimal experimental design for diffusion kurtosis imaging. *IEEE Trans Med Imaging*. 2010;29:819-829.
14. Ankele M, Schultz T. Quantifying microstructure in fiber crossings with diffusional kurtosis. In: *Proc. Medical Image Analysis and Computer-Aided Intervention (MICCAI) Part I; 9349 of LNCS*. Berlin Heidelberg: Springer; 2015:52-60.
15. Pajevic S, Pierpaoli C. Color schemes to represent the orientation of anisotropic tissues from diffusion tensor data: application to white matter fiber tract mapping in the human brain. *Magn Reson Med*. 1999;42:526-540.
16. Demiralp C, Hughes JF, Laidlaw DH. Coloring 3D line fields using Boy's real projective plane immersion. *IEEE Trans Vis Comput Graphics*. 2009;15:1457-1464.
17. Schlüter M, Rexilius J, Hahn HK, Peitgen HO, Stieltjes B. Unique planar color coding of fiber bundles and its application to fiber integrity quantification. In: *Proc 2004 IEEE International Symposium on Biomedical Imaging (ISBI)*. Vol. 2004. Arlington, VA, USA: IEEE; 900-903.
18. Ropinski T, Oeltze S, Preim B. Survey of glyph-based visualization techniques for spatial multivariate medical data. *Comput Graphics*. 2011;35:392-401.
19. Kindlmann G, Westin CF. Diffusion tensor visualization with glyph packing. *IEEE Trans Vis Comput Graphics*. 2006;12:1329-1335.
20. Pierpaoli C, Basser PJ. Toward a quantitative assessment of diffusion anisotropy. *Magn Reson Med*. 1996;36:893-906.
21. Schultz T, Kindlmann G. Superquadric glyphs for symmetric second-order tensors. *IEEE Trans Vis Comput Graphics*. 2010;16:1595-1604.
22. Kindlmann G. Superquadric tensor glyphs. In: Deussen O, Hansen C, Keim D, Saupe D, eds. *Proceedings of the Joint Eurographics - IEEE TCVG Symposium on Visualization ('VisSym')*. Aire-la-Ville, Switzerland: Eurographics Association; 2004:147-154.
23. Hlawitschka M, Eichelbaum S, Scheuermann G. Fast and memory efficient GPU-based rendering of tensor data. In: *Proc IADIS Computer Graphics and Visualization*. IADIS; 2008.
24. Wedeen VJ, Hagmann P, Tseng WYI, Reese TG, Weisskoff RM. Mapping complex tissue architecture with diffusion spectrum magnetic resonance imaging. *Magn Reson Med*. 2005;54:1377-1386.
25. Tuch DS. Q-Ball imaging. *Magn Reson Med*. 2004;52:1358-1372.
26. Tournier JD, Calamante F, Gadian DG, Connelly A. Direct estimation of the fiber orientation density function from diffusion-weighted MRI data using spherical deconvolution. *Neuroimage*. 2004;23:1176-1185.
27. Hashash YMA, Yao JIC, Wotring DC. Glyph and hyperstreamline representation of stress and strain tensors and material constitutive response. *Int J Numer Anal Methods Geomech*. 2003;27:603-626.
28. Özarslan E, Mareci T. Generalized diffusion tensor imaging and analytical relationships between diffusion tensor imaging and high angular resolution diffusion imaging. *Magn Reson Med*. 2003;50:955-965.
29. Peeters T, Prčkovska V, Almsick M, Vilanova A, Haar Romeny B. Fast and sleek glyph rendering for interactive HARDI data exploration. In: *Proc IEEE Pacific Vis Symposium*. Piscataway, NJ: IEEE; 2009:153-160.
30. Barmpoutis A, Vemuri BC, Howland D, Forder JR. Extracting tractosemas from a displacement probability field for tractography in DW-MRI. In: Metaxas D, et al, ed. *Proc Medical Image Computing and Computer-Assisted Intervention (MICCAI); 5241 of LNCS*. Berlin Heidelberg: Springer; 2008:9-16.
31. Schultz T. Towards resolving fiber crossings with higher order tensor inpainting. In: Laidlaw DH, Vilanova A, eds. *New Developments in the Visualization and Processing of Tensor Fields*. Berlin Heidelberg: Springer; 2012:253-265.
32. Schultz T, Kindlmann G. A maximum enhancing higher-order tensor glyph. *Comput Graphics Forum*. 2010;29:1143-1152.
33. Raffelt D, Tournier JD, Rose S, et al. Apparent fibre density: A novel measure for the analysis of diffusion-weighted magnetic resonance images. *Neuroimage*. 2012;59:3976-3994.
34. Almsick M, Peeters THJM, Prčkovska V, Vilanova A, Haar Romeny BM. GPU-based ray-casting of spherical functions applied to high angular resolution diffusion imaging. *IEEE Trans Vis Comput Graphics*. 2011;17:612-625.
35. Shattuck DW, Chiang MC, Barysheva M, et al. Visualization tools for high angular resolution diffusion imaging. In: Metaxas D, et al, ed. *Proc Medical Image Computing and Computer-Assisted Intervention (MICCAI); 5242 of LNCS*. Berlin Heidelberg: Springer; 2008:298-305.
36. Schultz T, Fuster A, Ghosh A, Deriche R, Florack L, Lim LH. Higher-order tensors in diffusion imaging. In: Westin CF, Vilanova A, Burgeth B, eds. *Visualization and Processing of Tensors and Higher Order Descriptors for Multi-Valued Data*. Berlin Heidelberg: Springer; 2014:129-161.

37. Gleicher M, Albers D, Walker R, Jusufi I, Hansen CD, Roberts JC. Visual comparison for information visualization. *Inf Vis*. 2011;10:289-309.
38. Hotz I, Sreevalsan-Nair J, Hagen H, Hamann B. Tensor field reconstruction based on eigenvector and eigenvalue interpolation. *Dagstuhl Follow-Ups*. 2010;1.
39. Schultz T, Schlaffke L, Schölkopf B, Schmidt-Wilcke T. HiFIVE: a Hilbert space embedding of fiber variability estimates for uncertainty modeling and visualization. *Comput Graphics Forum*. 2013;32:121-130.
40. Zhang C, Schultz T, Lawonn K, Eisemann E, Vilanova A. Glyph-based comparative visualization for diffusion tensor fields. *IEEE Trans. on Visualization and Computer Graphics*. 2016;22(1):797-806.
41. Jones DK, Griffin LD, Alexander DC, et al. Spatial normalization and averaging of diffusion tensor MRI data sets. *Neuroimage*. 2002;17:592-617.
42. Abbasloo A, Wiens V, Hermann M, Schultz T. Visualizing tensor normal distributions at multiple levels of detail. *IEEE Trans Vis Comput Graphics*. 2016;22:975-984.
43. Chung S, Lu Y, Henry RG. Comparison of bootstrap approaches for estimation of uncertainties of DTI parameters. *Neuroimage*. 2006;33:531-541.
44. Wittenbrink CM, Pang AT, Lodha SK. Glyphs for visualizing uncertainty in vector fields. *IEEE Trans Vis Comput Graphics*. 1996;2:266-279.
45. Jones DK. Determining and visualizing uncertainty in estimates of fiber orientation from diffusion tensor MRI. *Magn Reson Med*. 2003;49:7-12.
46. Wiens V, Schlaffke L, Schmidt-Wilcke T, Schultz T. Visualizing uncertainty in HARDI tractography using superquadric streamtubes. In: *Proc EG Conf on Visualization (EuroVis) Short Papers*. Aire-la-Ville, Switzerland: Eurographics Association; 2014:37-41.
47. Basser PJ, Pajevic S. Spectral decomposition of a 4th-order covariance tensor: Applications to diffusion tensor MRI. *Signal Process*. 2007;87:220-236.
48. Jiao F, Phillips JM, Gur Y, Johnson CR. Uncertainty visualization in HARDI based on ensembles of ODFs. In: Hauser H, Kobourov SG, Qu H, eds. *Proc IEEE Pacific Vis Symposium*. Piscataway, NJ: IEEE; 2012:193-200.
49. Jeurissen B, Descoteaux M, Mori S, Leemans A. Diffusion MRI fiber tractography of the brain. *NMR Biomed*. 2017;e3785. <https://doi.org/10.1002/nbm.3785>
50. Mori S, Crain BJ, Chacko VP, Zijl PCM. Three-dimensional tracking of axonal projections in the brain by magnetic resonance imaging. *Ann Neurol*. 1999;45:265-269.
51. Zöckler M, Stalling D, Hege HC. Interactive visualization of 3d-vector fields using illuminated stream lines. In: *Proc IEEE Visualization*. Piscataway, NJ: IEEE; 1996:107-114.
52. Basser PJ, Pajevic S, Pierpaoli C, Duda J, Aldroubi A. In vivo fiber tractography using DT-MRI data. *Magn Reson Med*. 2000;44:625-632.
53. Vist/e: Interactive visualization of DTI, HARDI and other complex imaging data. <https://sourceforge.net/projects/viste/>
54. Zhang S, Demiralp C, Laidlaw DH. Visualizing diffusion tensor MR images using streamtubes and streamsurfaces. *IEEE Trans Vis Comput Graphics*. 2003;9:454-462.
55. Delmarcelle T, Hesselink L. Visualizing second-order tensor fields with hyperstreamlines. *IEEE Comput Graph Appl*. 1993;13:25-33.
56. Stoll C, Gumhold S, Seidel HP. Visualization with stylized line primitives. In: Silva C, Gröller E, Rushmeier H, eds. *Proc IEEE Visualization*. Piscataway, NJ: IEEE; 2005:695-702.
57. Petrovic V, Fallon J, Kuester F. Visualizing whole-brain DTI tractography with GPU-based tuboids and LoD management. *IEEE Trans Vis Comput Graphics*. 2007;13:1488-1495.
58. Prčkovska V, Peeters THJM, Almsick M, Haar Romeny B, Vilanova A. Fused DTI/HARDI visualization. *IEEE Trans Vis Comput Graphics*. 2011;17:1407-1419.
59. Vos SB, Viergever MA, Leemans A. Multi-fiber tractography visualizations for diffusion MRI data. *PLOS ONE*. 2013;8:e81453.
60. Post FH, Vrolijk B, Hauser H, Laramée RS, Doleisch H. Feature extraction and visualisation of flow fields. In: *Eurographics 2002 - STARs*. Aire-la-Ville, Switzerland: Eurographics Association; 2002.
61. Vilanova A, Berenschot G, Pul C. DTI visualization with stream surfaces and evenly-spaced volume seeding. In: Deussen O, Hansen C, Keim DA, Saupe D, eds. *Proc Joint Eurographics - IEEE TCVG Symposium on Visualization (VisSym)*. Aire-la-Ville, Switzerland: Eurographics Association; 2004:173-182.
62. Reina G, Bidmon K, Enders F, Hastreiter P, Ertl T. GPU-based hyperstreamlines for diffusion tensor imaging. In: Ertl T, Joy K, Santos B, eds. *Proc Eurographics/IEEE-VGTC Symposium on Visualization (EuroVis)*. Aire-la-Ville, Switzerland: Eurographics Association; 2006:35-42.
63. Merhof D, Sonntag M, Enders F, Nimsky C, Hastreiter P, Greiner G. Hybrid visualization for white matter tracts using triangle strips and point sprites. *IEEE Trans Vis Comput Graphics*. 2006;12:1181-1188.
64. Banks DC, Westin CF. Global illumination of white matter fibers from DT-MRI data. In: Linsen L, Hagen H, Hamann B, eds. *Visualization in Medicine and Life Sciences*. Berlin Heidelberg: Springer; 2008:173-184.
65. Eichelbaum S, Hlawitschka M, Scheuermann G. LineAO—improved three-dimensional line rendering. *IEEE Trans Vis Comput Graphics*. 2013;19:433-445.
66. Everts MH, Bekker H, Roerdink JBTM, Isenberg T. Depth-dependent halos: Illustrative rendering of dense line data. *IEEE Trans Vis Comput Graphics*. 2009;15:1299-1306.
67. Isenberg T. A survey of illustrative visualization techniques for diffusion-weighted MRI tractography. In: Hotz I, Schultz T, eds. *Visualization and Processing of Higher Order Descriptors for Multi-Valued Data*. Berlin Heidelberg: Springer; 2015:235-256.
68. Zhang S, Demiralp Ç, Keefe DF, et al. An immersive virtual environment for DT-MRI volume visualization applications: A case study. In: *Proc IEEE Visualization*. Piscataway, NJ: IEEE; 2001:437-440.
69. Chen J, Cai H, Auchus AP, Laidlaw DH. Effects of stereo and screen size on the legibility of three-dimensional streamtube visualization. *IEEE Trans Vis Comput Graphics*. 2012;18:2130-2139.
70. Laramée RS, Hauser H, Doleisch H, Vrolijk B, Post FH, Weiskopf D. The state of the art in flow visualization: Dense and texture-based techniques. *Comput Graphics Forum*. 2004;23:203-221.
71. Van Wijk JJ. Spot noise texture synthesis for data visualization. In: *ACM Siggraph Computer Graphics*. Vol. 25. New York, NY: ACM; 1991:309-318.
72. Cabral B, Leedom LC. Imaging vector fields using line integral convolution. In: *Proceedings of the 20th annual conference on Computer graphics and interactive techniques*. New York, NY: ACM; 1993:263-270.

73. Stalling D, Hege HC. Fast and resolution independent line integral convolution. In: *Proceedings of the 22nd annual conference on Computer graphics and interactive techniques*. New York, NY: ACM; 1995:249-256.
74. Van Wijk JJ. Image based flow visualization. In: *ACM Trans Graphics (TOG)*. Vol. 21. New York, NY: ACM; 2002:745-754.
75. Zheng X, Pang A. HyperLIC. In: *Proc IEEE Visualization*. Piscataway, NJ: IEEE; 2003:249-256.
76. Hotz I, Feng L, Hagen H, Hamann B, Joy K, Jeremic B. Physically based methods for tensor field visualization. In: *Visualization*. Piscataway, NJ: IEEE; 2004:123-130.
77. Interrante V, Grosch C. Strategies for effectively visualizing 3D flow with volume LIC. In: *Proceedings of the 8th conference on Visualization'97*. Piscataway, NJ: IEEE Computer Society Press; 1997:421-424.
78. Rezk-Salama C, Hastreiter P, Teitzel C, Ertl T. Interactive exploration of volume line integral convolution based on 3D-texture mapping. In: *Proceedings of the conference on Visualization'99: celebrating ten years*. Piscataway, NJ: IEEE Computer Society Press; 1999:233-240.
79. Hsu E. Generalized line integral convolution rendering of diffusion tensor fields. In: *Proceedings of the International Society for Magnetic Resonance in Medicine, 9th Scientific Meeting and Exhibition, Glasgow, UK*. Concord, CA: ISMRM; 2001:790.
80. Wünsche B. Advanced texturing techniques for the effective visualization of neuroanatomy from diffusion tensor imaging data. In: *Proc. Asia-Pacific Bioinformatics Conference (APBC)*. Kent Town, Australia: Australian Computer Society; 2004:303-308.
81. Eichelbaum S, Hlawitschka M, Hamann B, Scheuermann G. Image-Space Tensor Field Visualization Using a LIC-like Method. In: *Visualization in medicine and life sciences II*. Berlin Heidelberg: Springer; 2012:191-208.
82. Höller M, Otto KM, Klose U, Groeschel S, Ehrlicke HH. Fiber visualization with LIC maps using multidirectional anisotropic glyph samples. *J Biomed Imaging*. 2014;2014:14.401819.
83. Calamante F, Tournier JD, Jackson GD, Connelly A. Track-density imaging (TDI): super-resolution white matter imaging using whole-brain track-density mapping. *Neuroimage*. 2010;53:1233-1243.
84. Calamante F, Tournier JD, Heidemann RM, Anwender A, Jackson GD, Connelly A. Track density imaging (TDI): validation of super resolution property. *Neuroimage*. 2011;56:1259-1266.
85. Schultz T, Theisel H, Seidel HP. Crease surfaces: From theory to extraction and application to diffusion tensor MRI. *IEEE Trans Vis Comput Graphics*. 2010;16:109-119.
86. Wedeen VJ, Rosene DL, Wang R, et al. The geometric structure of the brain fiber pathways. *Science*. 2012;335:1628-1634.
87. Tax CM, Dela Haije T, Fuster A, et al. Sheet probability index (SPI): Characterizing the geometrical organization of the white matter with diffusion MRI. *Neuroimage*. 2016;142:260-279.
88. Tax CMW, Westin CF, Dela Haije T, et al. Quantifying the brain's sheet structure with normalized convolution. *Med Image Anal*. 2017;39:162-177.
89. Ankele M, Schultz T. A sheet probability index from diffusion tensor imaging. In: Kaden E, Grussu F, Ning L, Tax CMW, Veraart J, eds. *Computational Diffusion MRI*. Berlin Heidelberg: Springer; 2018.
90. Jones DK, Travis AR, Eden G, Pierpaoli C, Basser PJ. PASTA: pointwise assessment of streamline tractography attributes. *Magn Reson Med*. 2005;53:1462-1467.
91. Behrens T, Woolrich M, Jenkinson M, et al. Characterization and propagation of uncertainty in diffusion-weighted MR imaging. *Magn Reson Med*. 2003;50:1077-1088.
92. Schultz T, Vilanova A, Brecheisen R, Kindlmann G. Fuzzy fibers: Uncertainty in dMRI tractography. In: Hansen C, Chen M, Johnson C, Kaufman A, Hagen H, eds. *Scientific Visualization: Uncertainty, Multifield, Biomedical, and Scalable Visualization*. Berlin Heidelberg: Springer; 2014:79-92.
93. Hagmann P, Thiran JP, Jonasson L, et al. DTI mapping of human brain connectivity: statistical fibre tracking and virtual dissection. *Neuroimage*. 2003;19:545-554.
94. Jones DK. Tractography gone wild: Probabilistic fibre tracking using the wild bootstrap with diffusion tensor MRI. *IEEE Trans Med Imaging*. 2008;27:1268-1274.
95. McGraw T, Nadar MS. Stochastic DT-MRI connectivity mapping on the GPU. *IEEE Trans Vis Comput Graphics*. 2007;13:1504-1511.
96. Enders F, Sauber N, Merhof D, Hastreiter P, Nimsky C, Stamminger M. Visualization of white matter tracts with wrapped streamlines. In: Silva C, Gröller E, Rushmeier H, eds. *Proc IEEE Visualization*. Piscataway, NJ: IEEE; 2005:51-58.
97. Schultz T, Theisel H, Seidel HP. Topological visualization of brain diffusion MRI data. *IEEE Trans Vis Comput Graphics*. 2007;13:1496-1503.
98. Schober M, Kasenburg N, Feragen A, Hennig P, Hauberg S. Probabilistic shortest path tractography in DTI using Gaussian process ODE solvers. In: *Proc Medical Image Computing and Computer-Assisted Intervention (MICCAI), Part III; 8675 of LNCS*. Berlin Heidelberg: Springer; 2014:265-272.
99. Brown CJ, Booth BG, Hamarneh G. Uncertainty in tractography via tract confidence regions. In: Schultz T, Nedjati-Gilani G, Venkataraman A, O'Donnell L, Panagiotaki E, eds. *Computational Diffusion MRI and Brain Connectivity*. Berlin Heidelberg: Springer; 2014:129-138.
100. Brecheisen R, Platel B, Haar Romenij BM, Vilanova A. Illustrative uncertainty visualization of DTI fiber pathways. *The Visual Computer*. 2013;29:297-309.
101. Brecheisen R, Vilanova A, Platel B, Haar Romenij BM. Parameter sensitivity visualization for DTI fiber tracking. *IEEE Trans Vis Comput Graphics*. 2009;15:1441-1448.
102. Jiao F, Gur Y, Johnson CR, Joshi S. Detection of crossing white matter fibers with high-order tensors and rank-k decompositions. In: Székely G, Hahn HK, eds. *IPMI*. 6801 of LNCS; Berlin Heidelberg: Springer; 2011:538-549.
103. Shneiderman B. The eyes have it: A task by data type taxonomy for information visualizations. In: *Visual Languages, 1996. Proceedings, IEEE Symposium on*. Piscataway, NJ: IEEE; 1996:336-343.
104. Wakana S, Jiang H, Nagae-Poetscher LM, Van Zijl PC, Mori S. Fiber tract-based atlas of human white matter anatomy 1. *Radiology*. 2004;230:77-87.
105. Blaas J, Botha CP, Peters B, Vos FM, Post FH. Fast and reproducible fiber bundle selection in DTI visualization. In: *Visualization, 2005. VIS 05. IEEE*. Piscataway, NJ: IEEE; 2005:59-64.
106. Köhn A, Klein J, Weiler F, Peitgen HO. A GPU-based fiber tracking framework using geometry shaders. *Proc SPIE Med Imaging*. 2009;7261:72611J.
107. Chamberland M, Whittingstall K, Fortin D, Mathieu D, Descoteaux M. Real-time multi-peak tractography for instantaneous connectivity display. *Front Neuroinform*. 2014;8:59.

108. Salzbrunn T, Scheuermann G. Streamline predicates. *IEEE Trans Vis Comput Graphics*. 2006;12:1601-1612.
109. Tax CMW, Chamberland M, Stralen M, et al. Seeing more by showing less: Orientation-dependent transparency rendering for fiber tractography visualization. *PLOS ONE*. 2015;10:1-20.
110. Sherbondy A, Akers D, Mackenzie R, Dougherty R, Wandell B. Exploring connectivity of the brain's white matter with dynamic queries. *IEEE Trans Vis Comput Graphics*. 2005;11:419-430.
111. Chen W, Ding ZA, Zhang S, et al. A novel interface for interactive exploration of DTI fibers. *IEEE Trans Vis Comput Graphics*. 2009;15:1433-1440.
112. Jianu R, Demiralp Ç, Laidlaw DH. Exploring 3D DTI fiber tracts with linked 2D representations. *IEEE Trans Vis Comput Graphics*. 2009;15:1449-1456.
113. Jianu R, Demiralp Ç, Laidlaw DH. Exploring brain connectivity with two-dimensional neural maps. *IEEE Trans Vis Comput Graphics*. 2012;18:978-987.
114. O'Donnell LJ, Westin CF. Automatic tractography segmentation using a high-dimensional white matter atlas. *IEEE Trans Med Imaging*. 2007;26:1562-1575.
115. Wassermann D, Bloy L, Kanterakis E, Verma R, Deriche R. Unsupervised white matter fiber clustering and tract probability map generation: Applications of a Gaussian process framework for white matter fibers. *Neuroimage*. 2010;51:228-241.
116. Chen W, Zhang S, Correia S, Ebert DS. Abstractive representation and exploration of hierarchically clustered diffusion tensor fiber tracts. *Comput Graphics Forum*. 2008;27:1071-1078.
117. Otten R, Vilanova A, Van De Wetering H. Illustrative white matter fiber bundles. *Comput Graphics Forum*. 2010;29:1013-1022.
118. Schultz T, Theisel H, Seidel HP. Segmentation of DT-MRI anisotropy isosurfaces. In: Museth K, Möller T, Ynnerman A, eds. *Proc. Eurographics/IEEE-VGTC Symposium on Visualization (EuroVis)*. Aire-la-Ville, Switzerland: Eurographics Association; 2007:187-194.
119. Kindlmann G, Tricoche X, Westin CF. Delineating white matter structure in diffusion tensor MRI with anisotropy creases. *Med Image Anal*. 2007;11:492-502.
120. Eberly D. *Ridges in Image and Data Analysis; Computational Imaging and Vision 7*. Dordrecht: Kluwer Academic Publishers; 1996.
121. Tricoche X, Kindlmann G, Westin CF. Invariant crease lines for topological and structural analysis of tensor fields. *IEEE Trans Vis Comput Graphics*. 2008;14:1627-1634.
122. Kindlmann G, San José Estépar R, Smith SM, Westin CF. Sampling and visualizing creases with scale-space particles. *IEEE Trans Vis Comput Graphics*. 2009;15:1415-1424.
123. Barakat S, Andryscio N, Tricoche X. Fast extraction of high-quality crease surfaces for visual analysis. *Comput Graphics Forum*. 2011;30:961-970.
124. Smith SM, Jenkinson M, Johansen-Berg H, et al. Tract-based spatial statistics: Voxelwise analysis of multi-subject diffusion data. *Neuroimage*. 2006;31:1487-1505.
125. Engel K, Hadwiger M, Kniss JM, Rezk-Salama C, Weiskopf D. *Real-Time Volume Graphics*. Baton Rouge: Taylor & Francis Ltd; 2006.
126. Kindlmann G, Weinstein D, Hart D. Strategies for direct volume rendering of diffusion tensor fields. *IEEE Trans Vis Comput Graphics*. 2000;6:124-138.
127. Bista S, Zhuo J, Gullapalli RP, Varshney A. Visualization of brain microstructure through spherical harmonics illumination of high fidelity spatio-angular fields. *IEEE Trans Visualization Comput Graphics*. 2014;20:2516-2525.
128. Vaillancourt O, Chamberland M, Houde JC, Descoteaux M. Visualization of diffusion propagator and multiple parameter diffusion signal. In: Hotz I, Schultz T, eds. *Visualization and Processing of Higher Order Descriptors for Multi-Valued Data*. Berlin Heidelberg: Springer; 2015.
129. Ledoux L-P, Houde J-C, Morency FC, Whittingstall K, Bélanger J-R, Descoteaux M. Fiberweb: a new web solution for medical visualization and interactions. In: *Proceedings of Breaking the Barriers of Diffusion MRI (ISMRM workshop)*. Concord, CA: ISMRM; 2016.
130. Gamwell L. *Mathematics and Art: A Cultural History*. Princeton, NJ: Princeton University Press; 2015.

How to cite this article: Schultz T, Vilanova A. Diffusion MRI visualization. *NMR in Biomedicine*. 2018;e3902. <https://doi.org/10.1002/nbm.3902>